Tropical mid-tropospheric CO_2 variability driven by the Madden–Julian oscillation

King-Fai Li[a,1], Baijun Tian[b], Duane E. Waliser[b], and Yuk L. Yung[a]

[a]Division of Geological and Planetary Sciences, California Institute of Technology, Pasadena, CA 91125; and [b]Jet Propulsion Laboratory, California Institute of Technology, Pasadena, CA 91109

Edited* by Richard M. Goody, Harvard, Falmouth, MA, and approved September 21, 2010 (received for review June 10, 2010)

Carbon dioxide (CO_2) is the most important anthropogenic greenhouse gas in the present-day climate. Most of the community focuses on its long-term (decadal to centennial) behaviors that are relevant to climate change, but there are relatively few discussions of its higher-frequency forms of variability, and none regarding its subseasonal distribution. In this work, we report a large-scale intraseasonal variation in the Atmospheric Infrared Sounder CO_2 data in the global tropical region associated with the Madden–Julian oscillation (MJO). The peak-to-peak amplitude of the composite MJO modulation is ~1 ppmv, with a standard error of the composite mean <0.1 ppmv. The correlation structure between CO_2 and rainfall and vertical velocity indicate positive (negative) anomalies in CO_2 arise due to upward (downward) large-scale vertical motions in the lower troposphere associated with the MJO. These findings can help elucidate how faster processes can organize, transport, and mix CO_2 and provide a robustness test for coupled carbon–climate models.

convection | intraseasonal variability | remote sensing

Discovered in ground-based observations of zonal wind and surface pressure anomalies in the 1970s, the Madden–Julian oscillation (MJO) is the most important tropical intraseasonal variability. The MJO is characterized by slow (~5 $m\,s^{-1}$) eastward-propagating, large-scale oscillations in tropical deep convection and baroclinic winds, especially over the warmest tropical waters in the equatorial Indian and western Pacific oceans during boreal winter (November–April) when the Indo-Pacific warm pool is centered near the equator (1–4). The MJO interacts with a number of weather and climate phenomena (4), atmospheric dynamics (5–7), ocean biology, and atmospheric chemical tracers (8–11). Our purpose is to examine the MJO's modulation of atmospheric carbon dioxide (CO_2).

CO_2 is the most important anthropogenic greenhouse gas in the present-day climate, contributing more than 50% of the total anthropogenic warming (12–14). Recently, the CO_2 mixing ratios in the middle troposphere (~5–10 km) have been retrieved using data from the Atmospheric Infrared Sounder (AIRS) aboard National Aeronautics and Space Administration (NASA)'s Aqua satellite (15–17). This seven-year global daily CO_2 dataset has shown rich variability with time scales from semiannual to interannual [e.g., El Niño–Southern oscillation (ENSO)] (17, 18), which helps improve our understanding of major processes that control the carbon exchange among reservoirs.

The AIRS Level 2 mid-tropospheric CO_2 product is retrieved using as input the AIRS Level 2 temperature, water vapor, and ozone geophysical products and selected channels of cloud-cleared radiances within the CO_2 absorption bands, i.e., 704–721 cm^{-1} (15–17). The spatial resolution at nadir is 90 km× 90 km, and the product is a column-weighted average of the CO_2 volume mixing ratio profile. At tropical latitudes, the weighting function peak occurs at 400 hPa (~7.5 km) and decreases to half its value at 120 hPa (~15 km) and 515 hPa (~5.5 km) (see figure 1 of ref. 15). Validation by comparison to in situ aircraft and ground-based measurements demonstrates that individual retrievals of AIRS CO_2 are accurate to better than 2 ppmv between latitudes 30 °S and 80 °N (17). The CO_2 Level 3 daily product employed in our analysis is an average of the individual Level 2 CO_2 retrievals over a 24-h span within a 2.5°-longitude × 2°-latitude grid. For latitudes between ±40°, the number of retrievals being averaged in each grid for each day ranges between zero to a maximum of 15, depending on the availability of at least three valid AIRS Level 2 retrievals in a 2 × 2 grouping of adjacent retrievals. This unprecedented AIRS mid-tropospheric CO_2 dataset provides great opportunity for climate studies and unique constraints for climate models. For example, based on the AIRS mid-tropospheric CO_2 data, it has been shown that convection in some of the chemistry–climate models has to be strengthened in order to reproduce observed CO_2 latitudinal gradient (19). In addition, the impact of changes in the Walker circulation over the central and western Pacific Ocean as a result of ENSO have been detected in the AIRS mid-tropospheric CO_2 data (18). For this reason, we expect that convection and large-scale vertical motion may also regulate CO_2 on the intraseasonal scale and AIRS mid-tropospheric CO_2 data may be able to reveal the MJO signal in CO_2.

Results

Fig. 1 shows the composite maps of the MJO-related mid-tropospheric CO_2 variation for eight commonly used phases of the MJO (20, 21) defined by the pair of all-season real-time multivariate MJO (RMM) indices (20). These maps are created using AIRS 2.5° × 2° gridded Level 3 CO_2 data during the boreal winters in November 2002–February 2010. Fig. S1 shows the (RMM_1, RMM_2) phase space for boreal winter from 2002 to 2010 to indicate the number of days for each phase of the composite MJO cycle. Only days with strong MJO activity ($RMM_1^2 + RMM_2^2 \geq 1$) are considered. Fig. S2 shows the number of daily, cloud-cleared data being averaged in the composite mean at different locations (see *Methods Summary* for details). To indicate the eastward propagation of the convective anomaly associated with the MJO, we overlaid the rainfall MJO anomalies from the Tropical Rainfall Measuring Mission (TRMM; solid/dotted contour lines) (22) in Fig. 1. The TRMM rainfall data we used cover the same period as AIRS and are interpolated onto the same 2.5° × 2° grids as AIRS. For improved visualization, a 10° longitude × 8° latitude running average is applied to both CO_2 and rainfall anomalies to remove high-wavenumber spatial fluctuations. In phase 1, a positive rainfall anomaly is found in the western equatorial Indian Ocean, indicating the presence of enhanced convection and rising air motion in this area. A significant positive anomaly in CO_2 (~ + 0.4 ppmv) is also apparent in this area. When the rising air mass reaches the upper troposphere, it diverges away from the cluster center and subsides in both east and west sides (e.g., Indonesia), where the air becomes relatively

Author contributions: K.-F.L., B.T., D.E.W., and Y.L.Y. designed research; K.-F.L. performed research; K.-F.L. analyzed data; and K.-F.L. wrote the paper.

The authors declare no conflict of interest.

*This Direct Submission article had a prearranged editor.

[1]To whom correspondence should be addressed. E-mail: kfl@gps.caltech.edu.

This article contains supporting information online at www.pnas.org/lookup/suppl/doi:10.1073/pnas.1008222107/-/DCSupplemental.

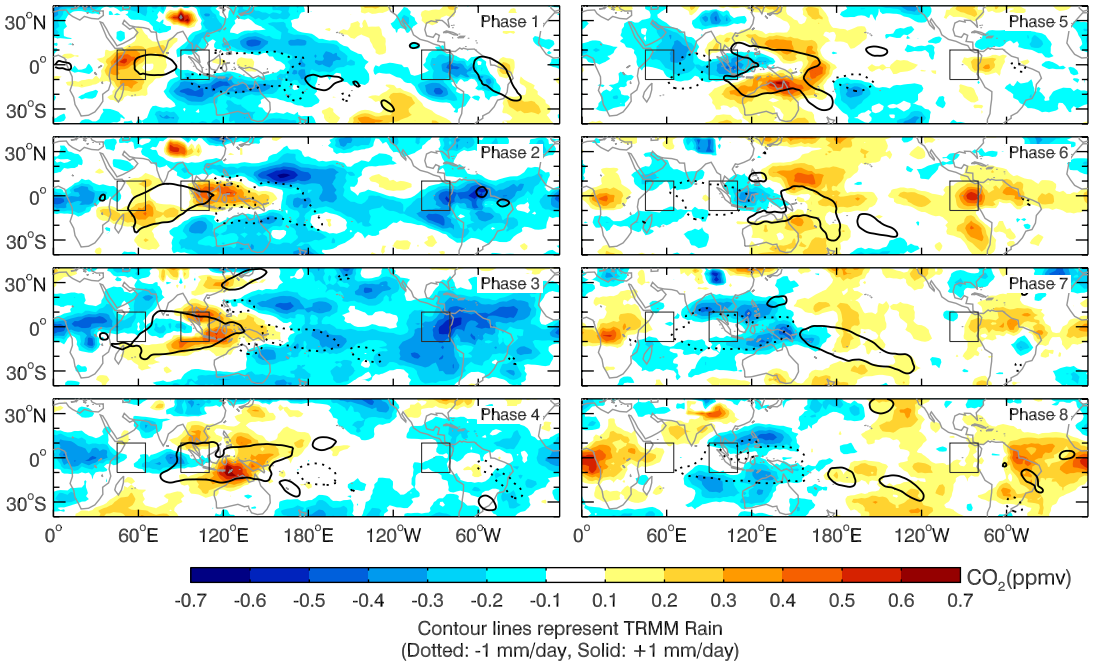

Fig. 1. MJO-related AIRS CO_2 anomalies. The MJO phase is defined using the All-season Real-time Multivariate MJO Index (RMM_1, RMM_2). Each phase represents a period of ~6 d. Only those days that satisfy $RMM_1^2 + RMM_2^2 \geq 1$ are included in the composite mean calculation. To indicate the propagation of the MJO, we overlaid the MJO-related rainfall anomaly using solid (dotted) contours for regions of values greater (lower) than $+1$ (-1) mm d^{-1}. The 20° × 20° square boxes enclose the representative regions for Fig. 5. For visualization, a 10°longitude × 8°latitude running average is applied to both CO_2 and rainfall anomalies to remove high-wavenumber spatial fluctuations.

drier and the convection is suppressed, as indicated by a negative rainfall anomaly. These dry areas show a negative anomaly (~ -0.4 ppmv) in AIRS CO_2, which extends all the way to the Eastern Pacific and South America, where the rainfall anomaly is small. In phases 2–4, the positive rainfall anomaly propagates eastward with a speed of ~5 m s^{-1}. The positive CO_2 anomaly also propagates eastward, and the propagation pattern is consistent with that of the rainfall. Meanwhile, there is a significant drop in CO_2 (~ -0.6 ppmv) over South America and central Africa, where the rainfall anomaly is weak. In phases 5–8, the enhanced convection moves from the Maritime Continent to the central Pacific, while the convection is suppressed in the Indian Ocean as indicated by a negative rainfall anomaly there. Meanwhile, the enhanced CO_2 ($\sim +0.3$ ppmv) propagates with the enhanced convection into the central Pacific. In addition, a positive CO_2 anomaly ($\sim +0.5$ ppmv) develops over the eastern Pacific and South America and it travels across the Atlantic Ocean to the central Africa. The speed of propagation in this relatively convection-free region is much faster (~20 m s^{-1}), yet consistent with the observed dynamical life cycle of the MJO (23). The anomaly continues to propagate into the Indian Ocean and the MJO cycle by inference repeats.

The main thermal infrared channels for CO_2 retrieval have some dependence on the presence of water vapor (H_2O), where a 10% error in water is estimated to cause a 1-ppmv bias in CO_2 (15). To examine any residual effects of H_2O in the retrieved CO_2, we show in Fig. 2 a scatter plot of all daily CO_2 and AIRS 550-hPa H_2O anomalies between 10 °S–10 °N, where the seasonal cycles are removed. The color contours represent the probability distribution function (PDF) of the scatter points. A least squares fit gives a slope of $\sim 0.13 \pm 0.01$ ppmv-CO_2 per g/kg-H_2O. If we assume that the slope is completely due to the retrieval bias from the H_2O absorption bands and assume that the MJO amplitude in H_2O at that level is ~1.4 g/kg (9), then the bias in CO_2 would be ~0.17 ppmv, which is much less than the signal we found above. Therefore, the MJO signal in AIRS CO_2 is unlikely an artifact of retrieval errors due to H_2O absorption.

Relations with Vertical Motions

The above comparison suggests that large-scale vertical motions may account for the MJO modulations in CO_2. Hence, to quantify their effects on the AIRS CO_2 variations, we compute the MJO-related pressure velocity anomalies at 700 hPa (ω_{700}) from the European Center for Medium-range Weather Forecasting (ECMWF) Interim reanalysis (ERA-interim) product covering the same period as AIRS. Furthermore, the ERA-interim data have been interpolated on the same 2.5° × 2° spatial grids as AIRS. For later discussion, we define the negative pressure velocity $\tilde{\omega}_{700} = -\omega_{700}$ such that positive (negative) $\tilde{\omega}_{700}$ refers to rising (sinking) motions. The $\tilde{\omega}_{700}$ anomalies from ERA-interim are shown in Fig. 3 (solid/dotted contours) and so are the CO_2 anomalies. For comparison, a 10°longitude × 8°latitude running average has also been applied. Over the Indian Ocean and the western Pacific, the MJO modulation of $\tilde{\omega}_{700}$ resembles that of AIRS CO_2, and they are positively correlated. Over the eastern Pacific and the American continents, the $\tilde{\omega}_{700}$ anomalies, though weak,

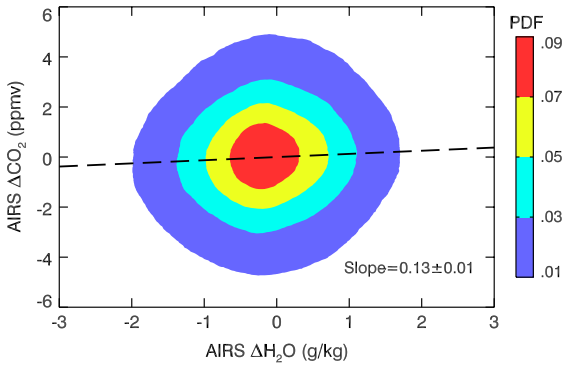

Fig. 2. Scatter plot of AIRS Level 3 CO_2 and H_2O daily anomalies during the winters of September 2002–November 2009 between 10 °S and 10 °N. Color contours represent the probability distribution function of the scattered points. The slope of the linear fit is 0.13 ± 0.01 ppmv-CO_2 per g/kg-H_2O.

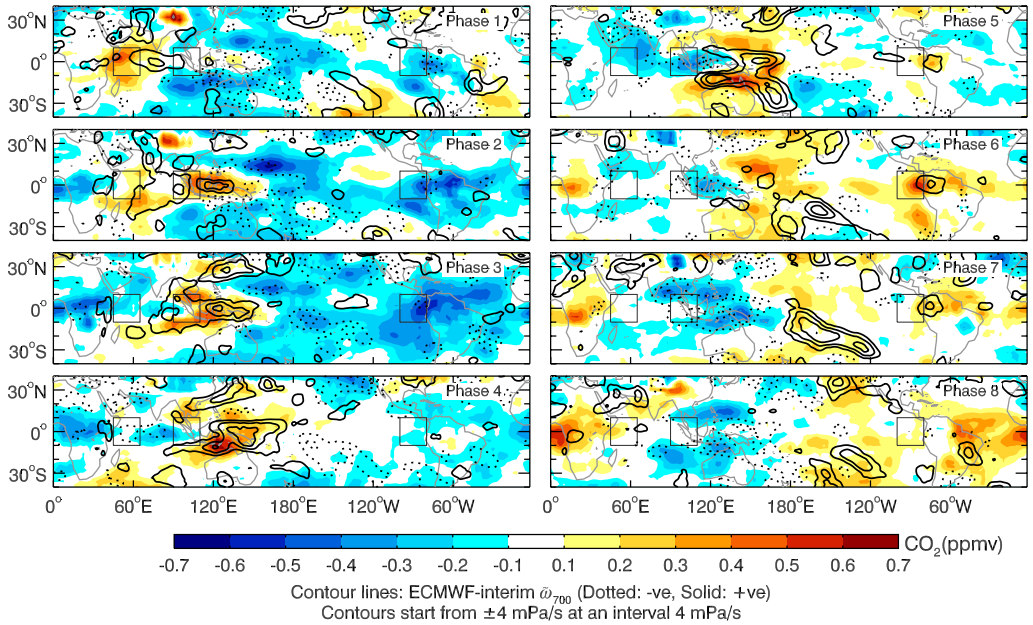

Fig. 3. Same as Fig. 1 except that ERA-interim 700-hPa pressure velocity anomalies $\tilde{\omega}_{700}$ are overlaid. The pressure velocity data cover the same period and have been interpolated to the same spatial grid as AIRS. Note that we redefined the pressure velocity such that positive (negative) values indicate rising (sinking) motions.

show some variations that are also consistent with the CO_2 anomalies (compare Fig. 3). Because of the uncertainty in the vertical velocity from reanalyses, we also show in Fig. S3 the $\tilde{\omega}_{700}$ anomalies from the National Centers for Environmental Prediction/National Center for Atmospheric Research (NCEP/NCAR) reanalysis. In general, the spatial-temporal patterns of $\tilde{\omega}_{700}$ anomalies from NCEP/NCAR reanalysis are consistent with those from ERA-interim and are also positively correlated with the AIRS CO_2 anomalies.

To further study their correlation, we compute the covariance of the MJO-modulated anomaly of CO_2 with that of $\tilde{\omega}_{700}$, which is shown in Fig. 4. It has been suggested that covariance or linear regression coefficients are more robust quantities than the correlation coefficients for filtered data (24). A positive covariance is generally seen over the western hemispheric oceans. It extends eastward from the equatorial western Indian Ocean, reaching a maximum (~2.5 ppmv mPa s^{-1}) over Indonesia, to the central Pacific. The southward movement of the covariance in the central Pacific resembles the characteristics of the MJO during boreal winters. In the eastern Pacific, there is a positive covariance (~1.3 ppmv mPa s^{-1}) near the coastline of Peru (0 °N, 80 °W). Overall, large-scale vertical motions in the lower troposphere are positively correlated with the MJO-related CO_2 anomalies.

To highlight the temporal variations in the variability of CO_2 and vertical motions, we show in Fig. 5 the time series in three representative regions over the western Indian Ocean, Indonesia, and the eastern Pacific Ocean. These regions are enclosed by 20° × 20° square boxes shown in Figs. 1 and 2 and Fig. S3. The eastward movement of the convective anomaly associated with the MJO is referenced by the rainfall anomaly. In general, these time series suggest a reasonably coherent MJO evolution between the relevant variables. The standard errors of the mean CO_2 variations, shown in blue shades, are of order ~0.02–0.05 ppmv. It is evident that the CO_2 anomaly exhibits roughly the same magnitudes (~0.5 ppmv) over all of the selected locations and is significantly different from zero at the 99% level or better, clearly showing its global effects. Over all three locations, the CO_2 variation is positively correlated with ERA-interim $\tilde{\omega}_{700}$. We note that the peak-to-peak amplitude of ERA-interim $\tilde{\omega}_{700}$ over Indonesia (~13 mPa s^{-1}) is about four times as strong as that over the other locations, likely due to the warmer sea-surface temperature. For comparison, the NCEP/NCAR $\tilde{\omega}_{700}$ anomalies are overlaid in Fig. 5. The $\tilde{\omega}_{700}$ variations from the two reanalyses are generally consistent with each other, although NCEP/NCAR $\tilde{\omega}_{700}$ is moderately stronger over the Indian Ocean and eastern Pacific. Moreover, there are some phase differences between NCEP/NCAR $\tilde{\omega}_{700}$ and CO_2 and between NCEP/NCAR $\tilde{\omega}_{700}$ and ERA-interim $\tilde{\omega}_{700}$. Thus, $\tilde{\omega}_{700}$ from both ERA-interim and NCEP/NCAR provide at least a qualitative picture that supports lower tropospheric vertical motions being an important driver of the MJO modulation on the mid-tropospheric CO_2.

Concluding Remarks

We have presented the observation of the MJO modulation in free-tropospheric CO_2. To date, there has been no attempt to simulate intraannual or interannual variability (e.g., ENSO) in atmospheric CO_2 (18). Thus the above observation provides a unique constraint as well as a robustness test for coupled carbon–climate models. The peak-to-peak amplitude is of order ~1 ppmv, which will have important implications on satellite measurements, such as NASA's Orbiting Carbon Observatory II and Japan Aerospace Exploration Agency's Greenhouse Gases Observing Satellite (GOSAT), that are designed to measure tropo-

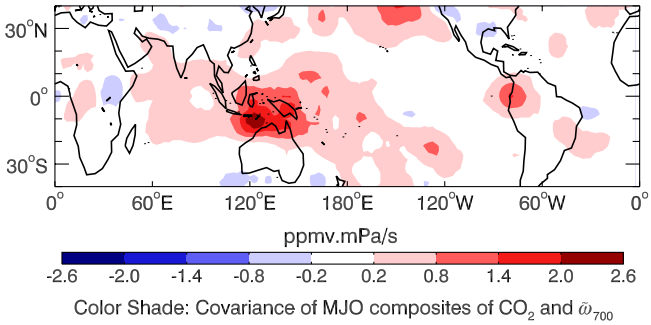

Fig. 4. The covariance between the MJO-related AIRS CO_2 and ERA-interim 700-hPa vertical velocity anomalies. A 10°longitude × 8°latitude running average has been applied. Positive covariance suggests that positive CO_2 anomalies are associated with enhanced upward motions, and vice versa.

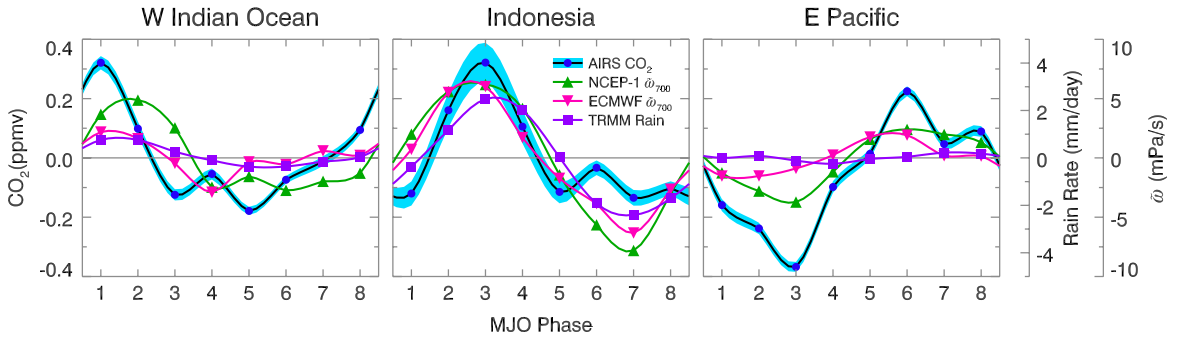

Fig. 5. Composite MJO time series of AIRS CO_2, reanalysis 700-hPa vertical velocity, and TRMM rainfall anomalies over the western Indian Ocean, Indonesia, and the eastern Pacific Ocean enclosed by the square boxes in Figs. 1 and 2 and Fig. S3. The blue bar overlaid on CO_2 shows the 99% confidence interval of the composite-mean uncertainty.

spheric CO_2 column with a precision better than 1 ppmv for determining carbon fluxes (25). It is also noted that for processes such as the MJO, the satellite instrument designs must account for cloud effects and the natural correlations between them and the moist processes and trace gases distributions that are so closely linked in order to accurately measure trace gas abundance in the lower atmosphere and under disturbed atmospheric conditions. This is likely to be achieved only through a multisensor framework that includes high spatial and spectral resolutions.

Our results also provide hints to the vertical distribution of CO_2. Because large-scale upward motions effectively transport air from the boundary layer to the free troposphere, on the time scale of about a day, the positive anomaly of AIRS CO_2 over regions with enhanced upward motion suggests that the surface CO_2 being brought up to the free troposphere has higher concentration than those in the free troposphere. Similarly, the negative anomaly over regions characterized by downward motion indicates that the sinking air from the free troposphere has lower CO_2. This seems to be generally true for the whole tropics. To verify this, the CO_2 averages of the National Oceanic and Atmospheric Administration (NOAA) Earth System Research Laboratory (ESRL) ground-based measurements in Guam (13.45 °N, 144.8 °E; pink line) (26) are compared with the Comprehensive Observation Network for Trace Gases by Airliner (CONTRAIL)'s airborne flask measurements in the free troposphere near the region (blue line) (27, 28) during boreal winters from 1994 to 2008 (Fig. 6). The CONTRAIL measurements are averaged between 5 °N–20 °N and 10–12 km. Guam is well-suited for this purpose because it is near the tropical warm pool region, where the MJO is active. Throughout the 15-year record, the ground CO_2 values are consistently higher by an average of 0.67± 0.26 ppmv (black dot with an error bar), which is of the same order of magnitude of the MJO anomalies shown in Fig. 1. The High-Performance Instrumented Airborne Platform for Environmental Research Pole-to-Pole Observations project, in which CO_2 concentrations and other trace gases at various latitudes in the Pacific basin are sampled between ∼1 km and 45 km, will provide another investigation of the CO_2 vertical profile in the Pacific regions.

Tropospheric CO_2 has also been measured by NASA's Tropospheric Emission Spectrometer and European Space Agency (ESA)'s Infrared Atmospheric Sounding Interferometer using thermal infrared channels similar to AIRS, ESA's Scanning Imaging Absorption Spectrometer for Atmospheric Cartography, and GOSAT using the CO_2 absorption bands in near-infrared, which characterize CO_2 at different altitudes. However, these data records are too short to provide a robust characterization of intraseasonal variability or have not yet been published. As these limitations are overcome, these independent datasets would combine to give collocated, vertical profiles of CO_2 and help confirm our findings.

Methods Summary

In Figs. 1 and 2 and Fig. S3, we defined the phase of the MJO using the RMM index (20). The RMM index consists of a pair of principal component time series, called RMM_1 and RMM_2, which are the projection of the daily observed NOAA outgoing longwave radiation (OLR) and NCEP/NCAR reanalysis and/or Australian Bureau of Meteorology Research Center Global Analysis and Prediction analysis 850- and 200-hPa zonal winds, with the annual cycle and components of interannual variability removed, on a pair of multiple-variable empirical orthogonal functions (EOFs). Two such EOFs are the leading pair of EOFs of the combined daily intraseasonal filtered fields of near-equatorially averaged (15 °S–15 °N) NOAA OLR and NCEP/NCAR 850- and 200-hPa zonal winds for all seasons from 1979 to 2001 (23 y) and describe the key features of the MJO. Fig. S1 shows the (RMM_1, RMM_2) phase space for all days in boreal winter from November 2002 to February 2010 and the number of days for each phase of the composite MJO cycle. Only days with strong MJO activity ($RMM_1^2 + RMM_2^2 \geq 1$) are considered. In general, the number of days in each phase of the composite MJO cycle ranges from 80 to 140 d. Noting that depending on the local cloud conditions, there may be zero or multiple CO_2 retrievals at each grid point on each individual day, the number of CO_2 retrievals being averaged in each phase of the composite MJO cycle (N_q) may range from ∼10 for cloudy regions (e.g., eastern Indian Ocean) to ∼500 for cloud-free regions (e.g., eastern Pacific; Fig. S2). The same method was applied to the time series shown in Fig. 5, except that the composite means were calculated

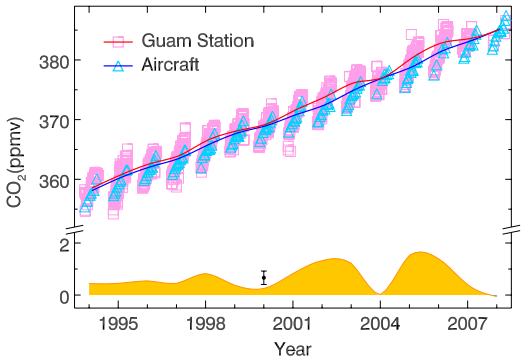

Fig. 6. Comparison of CO_2 winter averages from 1994 to 2008 between NOAA ESRL ground station (pink line) and CONTRAIL airborne flask measurements (blue line) over Guam (13.45 °N, 144.8 °E). Each square or triangle represents an individual measurement being used. During each flight, an individual airborne measurement shown in the figure is defined as an average of all flask measurements conducted between 5 °N–20 °N and 10–12 km. The yellow-filled area shows the ground-station values subtracted by the aircraft ones. The 15-y averaged difference is 0.67 ± 0.26 ppmv (black dot with an error bar).

using all daily data satisfying the above criteria in the $20° \times 20°$ square boxes. The total number of CO_2 retrievals $\tilde{N}_q$ being averaged in each square box is thus the sum of N_q over all the individual grid points within that box: $\tilde{N}_q = \sum_{20°\times20°\text{grid box}} N_q$. The critical value α for 99% confidence interval was derived from a two-tailed Student's t statistics, where the degree of freedom was $\tilde{N}_q - 1$. The 99% confidence interval was given by $(\tilde{\mu} - \alpha\frac{\tilde{\sigma}}{\sqrt{\tilde{N}_q}}, \tilde{\mu} + \alpha\frac{\tilde{\sigma}}{\sqrt{\tilde{N}_q}})$, where $\tilde{\mu}$ and $\tilde{\sigma}$ are the mean and the standard deviation of the data being averaged. Over the western Indian Ocean and the eastern Pacific Ocean, $\tilde{N}_q$ ranges from 5,000 to 8,000, and the standard errors of the sample means at 99% level, $\alpha\tilde{\sigma}/\sqrt{\tilde{N}_q}$, of the CO_2 composite means are thus ~0.02 ppmv. Because the region near Indonesia is relatively cloudy, $\tilde{N}_q$ drops to 2,000–5,000. Consequently, the standard errors of the sample means over Indonesia are ~0.05 ppmv.

ACKNOWLEDGMENTS. We thank Dr. Moustafa T. Chahine, Dr. Edward T. Olsen, and Mr. Luke Chen of the AIRS Science Team for providing information on the quality of AIRS data and comments on this work. We also thank Miss Le Kuai, Mr. Michael R. Line, Mr. Da Yang, Dr. Hartmut H. Aumann, Dr. David Crisp, Prof. Andrew P. Ingersoll, Prof. Xun Jiang, Dr. Brian H. Kahn, Dr. Susan S. Kulawik, Dr. Jack S. Margolis, Dr. Run-Lie Shia, Prof. Ka-Kit Tung, Dr. John R. Worden, and two anonymous reviewers for reviewing the manuscript and providing useful comments. This research was supported in part by National Science Foundation (NSF) Grant ATM-0840787 and Grant ATM-0934303 to the California Institute of Technology and NSF Grant ATM-0840755 to University of California, Los Angeles. Y.L.Y. was supported by Jet Propulsion Laboratory Grant P765982 to the California Institute of Technology. Part of this research was carried out at the Jet Propulsion Laboratory, California Institute of Technology, under a contract with the National Aeronautics and Space Administration. AIRS Level 3 daily CO_2 products were obtained from AIRS Data Server (http://disc.sci.gsfc.nasa.gov/AIRS/data-holdings/by-data-product/AIRX3C2D). AIRS Level 3 daily H_2O products were obtained from AIRS Data Server (http://disc.sci.gsfc.nasa.gov/AIRS/data-holdings/by-data-product/airsL3_STD_AIRS_AMSU.shtml). NCEP/NCAR reanalysis data used in this study were provided by the NOAA/Office of Oceanic and Atmospheric Research (OAR)/ESRL Physical Sciences Division (PSD) Data Server (http://www.esrl.noaa.gov/psd/data/reanalysis/). ERA-interim reanalysis data used in this study were obtained from the ECMWF Data Server (http://data.ecmwf.int/data/). The NOAA ESRL CO_2 data from the Carbon Cycle Cooperative Global Air Sampling Network, 1968–2008, Version 2009-07-15, were obtained from the NOAA FTP server (ftp://ftp.cmdl.noaa.gov/ccg/co2/flask/event/). CONTRAIL data were obtained from the World Meteorological Organization World Data Centre for Greenhouse Gases (http://gaw.kishou.go.jp/cgi-bin/wdcgg/accessdata.cgi). RMM indices were obtained from http://www.cawcr.gov.au/bmrc/clfor/cfstaff/matw/maproom/RMM/.

1. Madden RA, Julian PR (1971) Detection of a 40–50 day oscillation in zonal wind in tropical Pacific. *J Atmos Sci* 28:702–708.
2. Madden RA, Julian PR (1972) Description of global-scale circulation cells in tropics with a 40–50 day period. *J Atmos Sci* 29:1109–1123.
3. Zhang CD (2005) Madden-Julian oscillation. *Rev Geophys* 43:RG2003 10.1029/2004RG000158.
4. Lau WKM, Waliser DE (2006) *Intraseasonal Variability in the Atmosphere-Ocean Climate System* (Springer, New York) p 436.
5. Hendon HH, Salby ML (1994) The life-cycle of the Madden-Julian oscillation. *J Atmos Sci* 51:2225–2237.
6. Knutson TR, Weickmann KM (1987) 30–60 day atmospheric oscillations: Composite life cycles of convection and circulation anomalies. *Mon Weather Rev* 115:1407–1436.
7. Jiang X, et al. (2009) Vertical heating structures associated with the MJO as characterized by TRMM estimates, ECMWF reanalyses, and forecasts: A case study during 1998/99 winter. *J Climate* 22:6001–6020.
8. Waliser DE, Murtugudde R, Strutton P, Li JL (2005) Subseasonal organization of ocean chlorophyll: Prospects for prediction based on the Madden-Julian oscillation. *Geophys Res Lett* 32:L23602 10.1029/2005GL024300.
9. Tian BJ, et al. (2006) Vertical moist thermodynamic structure and spatial-temporal evolution of the MJO in AIRS observations. *J Atmos Sci* 63:2462–2485.
10. Tian BJ, et al. (2007) Intraseasonal variations of the tropical total ozone and their connection to the Madden-Julian oscillation. *Geophys Res Lett* 34:L08704 10.1029/2007GL029451.
11. Tian BJ, et al. (2008) Does the Madden-Julian oscillation influence aerosol variability? *J Geophys Res-Atmos* 113:D12215 10.1029/2007JD009372.
12. Quay PD, Tilbrook B, Wong CS (1992) Oceanic uptake of fossil fuel CO_2: Carbon-13 evidence. *Science* 256:74–79.
13. Francey RJ, et al. (1999) A 1000-year high precision record of $\delta^{13}C$ in atmospheric CO_2. *Tellus B* 51:170–193.
14. IPCC (2007) *Climate Change 2007: The Physical Science Basis. Contribution of Working Group I to the Fourth Assessment Report of the Intergovernmental Panel on Climate Change* (Cambridge Univ Press, Cambridge, UK) p 996.
15. Chahine M, Barnet C, Olsen ET, Chen L, Maddy E (2005) On the determination of atmospheric minor gases by the method of vanishing partial derivatives with application to CO_2. *Geophys Res Lett* 32:L22803 10.1029/2005GL024165.
16. Chahine MT, et al. (2006) Improving weather forecasting and providing new data on greenhouse gases. *Bull Am Meteorol Soc* 87:911–926.
17. Chahine MT, et al. (2008) Satellite remote sounding of mid-tropospheric CO_2. *Geophys Res Lett* 35:L17807 10.1029/2008GL035022.
18. Jiang X, Chahine MT, Olsen ET, Chen LL, Yung YL (2010) Interannual variability of mid-tropospheric CO_2 from Atmospheric Infrared Sounder. *Geophys Res Lett* 37:L13801.
19. Jiang X, et al. (2008) Simulation of upper tropospheric CO_2 from chemistry and transport models. *Global Biogeochem Cycles* 22:GB4025 10.1029/2007GB003049.
20. Wheeler MC, Hendon HH (2004) An all-season real-time multivariate MJO index: Development of an index for monitoring and prediction. *Mon Weather Rev* 132:1917–1932.
21. Waliser D, et al. (2009) MJO simulation diagnostics. *J Climate* 22:3006–3030.
22. Huffman GJ, et al. (2007) The TRMM multisatellite precipitation analysis (TMPA): Quasi-global, multiyear, combined-sensor precipitation estimates at fine scales. *J Hydrometeorol* 8:38–55.
23. Hendon HH, Salby ML (1996) Planetary-scale circulations forced by intraseasonal variations of observed convection. *J Atmos Sci* 53:1751–1758.
24. Coughlin KT, Tung KK (2006) Misleading patterns in correlation maps. *J Geophys Res-Atmos* 111:D24102 10.1029/2006JD007452.
25. Rayner PJ, O'Brien DM (2001) The utility of remotely sensed CO_2 concentration data in surface source inversions. *Geophys Res Lett* 28:175–178 10.1029/2000GL011912.
26. Conway TJ, Tans PP, Waterman LS, Thoning KW (1994) Evidence for interannual variability of the carbon-cycle from the NOAA/CMDL Global-Air-Sampling-Network. *J Geophys Res-Atmos* 99:22831–22855 10.1029/94JD01951.
27. Matsueda H, Inoue HY, Ishii M (2002) Aircraft observation of carbon dioxide at 8–13 km altitude over the western Pacific from 1993 to 1999. *Tellus B* 54:1–21.
28. Machida T, et al. (2008) Worldwide measurements of atmospheric CO_2 and other trace gas species using commercial airlines. *J Atmos Ocean Technol* 25:1744–1754.